Received: 6 March 2021 | Revised: 25 May 2021 | Accepted: 26 May 2021

DOI: 10.1002/er.6940

SHORT COMMUNICATION

INTERNATIONAL JOURNAL OF ENERGY RESEARCH WILEY

One-step synthesis of anionic S-substitution toward $Ni_2P(S)$ nanowires on nickel foam for enhanced hydrogen evolution reaction

Jie Xu[1,2] | **Tongtong Li**[3] | **Long Zhang**[4] | **Bing He**[1,2] | **Delong Feng**[1,2] | **Yun Zhou**[1,2]

[1]School of Medical Information and Engineering, Southwest Medical University, Luzhou, China

[2]Medicine & Engineering & Information Fusion and Transformation Key Laboratory of Luzhou City, Luzhou, China

[3]State Key Laboratory for Mechanical Behavior of Materials, School of Materials Science and Engineering, Xi'an Jiaotong University, Xi'an, China

[4]School of Materials Engineering, Xi'an Aeronautical University, Xi'an, China

Correspondence
Yun Zhou, School of Medical Information and Engineering, Southwest Medical University, Luzhou 646000, China.
Email: yzhou@swmu.edu.cn

Funding information
Natural Science Foundation of Shaanxi Province, Grant/Award Number: 2020JQ-386; Natural Science Foundation of Sichuan Province, Grant/Award Number: 14JC0124; the Science and Technology Strategic Cooperation Programs of Luzhou Municipal People's Government and Southwest Medical University, Grant/Award Number: 2019LZXNYDJ18

Summary

Hydrogen is considered a promising solution for energy, but the methods that are currently used in hydrogen production continue to rely on fossil fuels. Water electrolysis, a green and sustainable method for hydrogen production, is limited by the lack of nonprecious metal electrocatalysts that exhibit high performance. In this study, novel S-substituted Ni_2P nanowires with large aspect ratios were successfully grown on nickel foam ($Ni_2P(S)$/NF) using a facile one-step phosphating-sulfuration heat treatment process. The as-prepared $Ni_2P(S)$/NF exhibited enhanced activity in the hydrogen evolution reaction (HER) performed both in alkaline and acidic media. It only required overpotentials of 171 and 208 mV to drive current densities of 100 mA cm^{-2} in 1.0 M KOH solution and 0.5 M H_2SO_4, respectively. The characterization studies and density functional theory calculations suggested that the enhanced catalytic activity can be ascribed to the in situ growth of nanowires on nickel foam, the 1D nanowires morphology with high length-to-diameter ratio, appropriate free energy of hydrogen adsorption, and enhanced H_2O binding activity. This work will provide inspiration for the development of non-precious metal HER catalysts.

KEYWORDS

DFT calculation, hydrogen evolution reaction, novel morphology, S-substituted Ni_2P nanowires

1 | INTRODUCTION

Hydrogen is considered a promising solution for energy due to its advantages of high specific energy, low pollution and storability.[1,2] However, industrial methods that are currently used in hydrogen production continue to rely on fossil fuels, which exacerbates the problems of resource depletion and high carbon emissions.[3,4] Encouragingly, new energy power generation technologies and water electrolysis for the hydrogen evolution reaction (HER) can provide a green and sustainable method to produce hydrogen.[5-7] However, the cost of hydrogen production using water electrolysis from renewable energy is much higher than that using fossil fuels.[3,8] Consequently, further reduction in the cost is of great significance. One effective strategy to reduce the cost is to develop efficient, stable and cost-effective electrocatalysts to replace the current noble metal Pt-based catalysts. To date, various

transition metal alloys,[9,10] sulfides,[11-13] phosphides,[14-16] nitrides,[17,18] and carbides[19,20] have attracted widespread interest as efficient and low-cost electrocatalysts suitable for the HER. Among them, transitional metal phosphides (TMPs), such as nickel phosphides, have received a significant amount of attention because of their hydrogenase-like reactivity, good conductive properties, and electrochemical stability.[21,22] Nevertheless, the electrocatalytic performance of TMPs leaves much to be desired when compared to Pt-based materials. Hence, there is a wide consensus on the need for improvement in the electrocatalytic performance of TMPs.

Elemental doping or substitution can improve the HER catalytic performance. The introduction of metal cations redistributes the valence electrons and offers two electron-donating active sites. Inspired by this mechanism, vanadium-doped Ni_2P nanosheets,[22] ternary $Ni_{2-x}Co_xP$,[14] Mo-doped Ni_2P nanowire,[23] ternary $Co_{0.5}Ni_{0.5}P$ wire-on-flake heterostructure[15] and other transition metal doped or substituted structures were successfully synthesized. As expected, all of these materials exhibit increased catalytic activity. However, there are few studies on the substitution of non-metal elements in nickel phosphides, most of which are heterostructures.[24-26] Some studies suggest that substituting nonmetal elements may optimize the free energy of hydrogen adsorption (ΔG_{H^*}). For example, the synergy between S and P results in enhanced thermo-neutral electron/ion adsorption for the HER.[27,28] Sun et al used density functional theory (DFT) calculations to evaluate the change in ΔG_{H^*} when P was introduced into CoS_2 to form CoSP. They found that the ΔG_{H^*} of CoSP was almost thermo-neutral and confirmed using experimental studies that CoSP was a very promising HER catalyst.[29] Pan et al have prepared a heterogeneous nickel phosphide/sulfide electrocatalyst consisting of Ni_2P and Ni_3S_2. They found that the strong interactions between Ni_2P and Ni_3S_2 can optimize the electronic structure and adjust the hydrogen adsorption energy, thus significantly improving the catalytic activity.[28] Therefore, the substitution of S with nickel phosphides, such as Ni_2P, may improve the catalytic performance.

On the other hand, morphology tailoring has an important effect on the catalytic performance. Researchers have been committed to designing a variety of nanostructured electrode materials to take advantage of their morphology in catalysis.[30,31] For instance, Liu et al fabricated densely packed, vertically aligned Co-Ni-P nanowire arrays on nickel foam and suggested that the unique porous nanowire morphology was one of the important reasons for the excellent catalytic performance observed.[32] Kuang et al synthesized pure phase nickel $NiMoP_2$ nanowires on carbon cloth as an efficient and durable catalyst for water splitting. The large active surface area and good electron transport properties can be attributed to the architecture of the nanowires grown on the 3D substrate.[33] Hence, it is highly desirable to fabricate S-substituted nickel phosphide 1D structures with a large aspect ratio on 3D conductive substrates for further improving the catalytic performance. This configuration not only provides high-speed pathways for electron transfer but also contributes to the desorption of hydrogen bubbles accumulated on the surface of the catalysts,[21,34] thus increasing the contact area between the active sites and electrolyte.

Based on the aforementioned considerations, herein, novel S-substituted Ni_2P nanowire with a large aspect ratio was successfully grown on nickel foam (labelled as $Ni_2P(S)$/NF) suing a heat-phosphating-sulfurised NF prepared via a one-step, low temperature synthesis. The hydrogen adsorption free energy and H_2O binding activity of $Ni_2P(S)$ were optimized owing to the introduction of S atoms. Moreover, the structure of 1D nanowires grown in situ on the 3D porous substrate can expose abundant active sites and favor the release of bubble generated in the reaction. As expected, $Ni_2P(S)$/NF displayed excellent HER catalytic performance. This work sheds some light on exploring low-cost, efficient, and stable electrocatalysts for large-scale hydrogen production using water electrolysis.

2 | EXPERIMENTAL

2.1 | Materials and reagents

Red phosphorus (99.999%), sublimed sulfur (99.95%), potassium hydroxide (EL), ethanol (AR), hydrochloric acid (AR), acetone (AR), sodium hypophosphite monohydrate (99%) and commercial Pt/C (20 wt%) were purchased and used directly with any subsequent treatment. The surface oxides on nickel foam (NF) were removed via ultrasonication prior to use.

2.2 | Synthetic procedures

A facile one-step heat treatment process was used to prepare $Ni_2P(S)$/NF. First, the cleaned NF and S/P source were placed at the ends of a special porcelain boat, which was partitioned into unequal halves using a baffle. The S/P source was a mixed powder composed of fully ground S powder (0.4 g) and powder (0.4 g). Subsequently, the porcelain boat was placed in the central position of a tubular furnace. It should be noted that one end of the loaded NF was on the downstream side. After removing

the air in the tube under a flow of argon, the furnace was heated to 200°C for 10 minutes cooled to 50°C, and then heated to 350°C for 1 hour. Finally, the mixture was cooled in the furnace to room temperature. The as-prepared sample was then washed several times with distilled water and ethanol, respectively. The curve of the heat treatment process is shown in Figure S1. In contrast, Ni_2P on NF (Ni_2P/NF) was prepared using only $NaH_2PO_2{\cdot}H_2O$ heated at 300°C for 3 hours.

2.3 | Characterization

X-ray diffraction (XRD) on a PANAlytical instrument (Cu-Kα radiation) and X-ray photoemission spectrometry (XPS) on Kratos AXIS Ultra DLD instrument (Al Kα radiation) were employed to characterize the crystal structure and valence states. Field emission scanning electron microscopy (SEM) carried out on a Merlin Compact microscope and transmission electron microscopy (TEM) on a JEM-F200 instrument were used to observe the morphology of the as-prepared samples. The elemental composition was determined using energy-dispersive X-ray spectroscopy (EDS), which was equipped with the TEM instrument.

2.4 | Electrochemical tests

All electrochemical tests were performed on CorrTest CS350 electrochemical workstation using a standard three-electrode configuration with the as-prepared sample, Hg/HgO (for alkaline solution) or Ag/AgCl (for acid solution) electrode and graphite rod as the working, reference and auxiliary electrodes, respectively. Prior to measurements, N_2 gas was continuously bubbled through the electrolyte for tens of minutes. The H_2 evolution curves were recorded using linear sweep voltammetry in the potential range from 0.2 to −0.6 V (vs RHE) at a scan rate of 5 $mV{\cdot}s^{-1}$. Nyquist plots were obtained using electrochemical impedance spectroscopy (EIS) over the frequency range from 100 kHz to 1 Hz at a potential of −0.2 V vs RHE. The double-layer capacitance (C_{dl}) was derived using cyclic voltammetry (CV) at the scan rates of 4, 8, 12, 16, 20, 40 and 60 $mV{\cdot}s^{-1}$ in non-Faradaic region. The stability of Ni_2P(S)/NF was evaluated at a constant overpotential to achieve an initial current density of 50 $mA{\cdot}cm^{-2}$. All potentials in this work were converted to the reversible hydrogen electrode (RHE) potential using the following equation of $E_{RHE} = E_{Hg/HgO} + 0.098 + 0.059 \times pH$ (or $E_{RHE} = E_{Ag/AgCl} + 0.197 + 0.059 \times pH$), where E_{RHE} is the potential relative to RHE, $E_{Hg/HgO}$ and $E_{Ag/AgCl}$ are the measured potential relative to the Hg/HgO and Ag/AgCl electrode, respectively. Ohmic drop (iR) compensation was applied to all data unless stated otherwise.

2.5 | Simulation calculation

Simulation calculations were performed using DFT based on the Vienna Ab-initio Simulation Package (VASP) software package. The generalized gradient approximation, which was developed by Perdew-Burke-Ernzerhof, was employed to describe the electron exchange-correlation potential.[35] The Brillouin zones were sampled using the Monkhorst-Pack scheme with a $2 \times 2 \times 1$ k-point grid. The convergence tolerance of energy, maximum force and maximum displacement were set to 10^{-5} Ha, 0.002 Ha/Å and 0.005 Å, respectively. The van der Waals forces were removed using the DFT + D method within the Grimme scheme.[36] The adsorption of H and H_2O was studied to provide a theoretical basis for the electrocatalytic performance. The Gibbs-free adsorption energies were calculated using the following equation: $\Delta G_{ads} = \Delta E_{ads} + \Delta E_{ZPE} - T\Delta S$, which was derived from $\Delta E_{ads} = E_{H\ or\ H_2O/sub} - E_{sub} - E_{H\ or\ H_2O}$. $E_{H\ or\ H_2O/sub}$ represents the total energy of the adsorption system, E_{sub} is the energy of Ni_2P(S) and E_H and E_{H_2O} are the energies of one isolated H atom and one isolated H_2O molecule, respectively. ΔE_{ZPE} is the difference in the zero-point energy. For entropy (S), only the vibrational components were considered.

3 | RESULTS AND DISCUSSION

Scheme 1 shows that S-substituted Ni_2P nanowires with a large aspect ratio can be grown in situ on nickel foam using a facile one-step heat treatment process. The fully ground P/S mixture and heat treatment process have a significant effect on the results. Under such conditions, the corresponding phase and morphology were obtained.

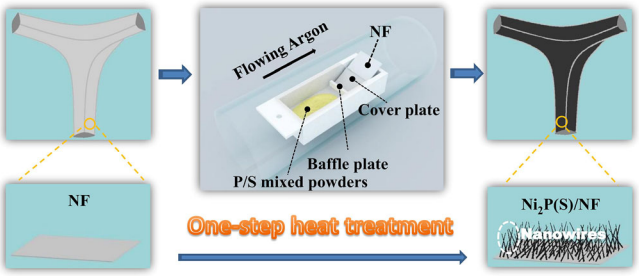

SCHEME 1 Scheme of the fabrication of Ni_2P(S)/NF [Colour figure can be viewed at wileyonlinelibrary.com]

The crystal structures of the as-obtained samples were characterized using XRD and the corresponding XRD patterns are shown in Figure 1 and Figure S2. It can be easily observed that the diffraction peaks of $Ni_2P(S)/NF$ are well indexed to those of Ni_2P (PDF#65-9706) with the exception that the peaks were shifted as a whole. In addition, no phase separation circumstances were observed. The XRD pattern obtained for $Ni_2P(S)/NF$ exhibited identical characteristic peaks to those of Ni_2P without other phosphides or sulfides, suggesting that the P sites in the Ni_2P crystal structure were partially replaced by S.[37] For comparative analysis, the simulated XRD pattern of $Ni_2P(S)$ is also shown in Figure 1. The calculation model was S-substituted Ni_2P with an S:P atomic ratio is 2:4. The results indicate that the diffraction peaks obtained for simulated $Ni_2P(S)$ can also be matched with those of Ni_2P (PDF#65-9706) and the as-prepared $Ni_2P(S)/NF$. The heat treatment of NF in the presence of $NaH_2PO_2{\cdot}H_2O$ at 300°C for 3 hours can obtain Ni_2P on NF (Figure S2), which is in accordance with the previous report.[26]

The morphologies and microstructures of the as-obtained samples were studied using SEM and TEM. Figure S3A shows that the NF possesses 3D porous structure, but after heat treatment with the S/P source, the NF surface was densely covered with uniform nanowires. It can be easily observed that the diameter of the as-obtained nanowires varies from 20 to 50 nm, while the lengths are in the range of 5 to 10 μm. This is a large aspect ratio. In addition, the as-prepared sample preserved the 3D macroporous foam morphology (Figure 2A-D). This morphology not only exposes abundant active sites but also favors the release of the bubble in the reaction. The single nanowire was further analyzed using TEM, as shown in Figure 2E. The corresponding high-resolution TEM image (Figure 2F) shows that the nanowire is single crystal, and the lattice fringe of 0.335 nm can be readily indexed to the (001) plane of Ni_2P. Moreover, elemental mapping under scanning TEM mode shows a uniform distribution of Ni, P and S in the nanowire (Figure 2G). The average atomic ratio of the nanowire was further estimated using TEM-EDS elemental mapping (Figure 2H). It indicates that the atomic ratio of Ni:(P + S) is close to 2:1, which satisfies the stoichiometry of Ni_2P. The result also suggest that approximately 35% of the P sites were substituted by S. Thus, it is reasonable to speculate that the phase composition of the nanowires were S-substituted Ni_2P ($Ni_2P(S)$) with no other phosphides or sulfides impurities when combined with the XRD. For comparison, the morphology of the sample prepared by calcining NF with only $NaH_2PO_2{\cdot}H_2O$ was determined, as shown in Figure S3B.

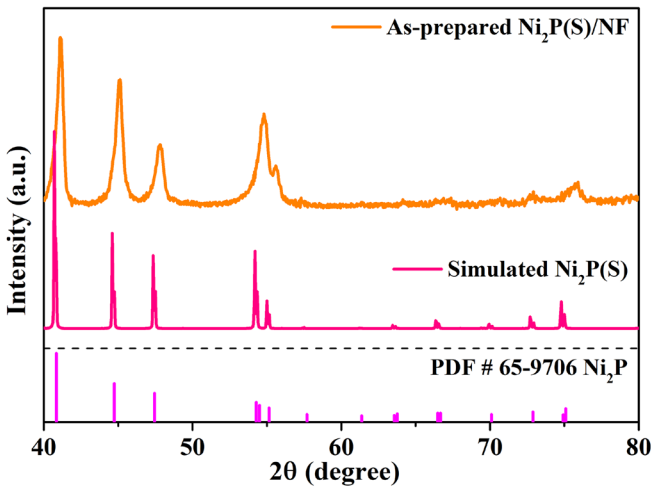

FIGURE 1 The X-ray diffraction (XRD) patterns of the simulated $Ni_2P(S)$ and as-prepared $Ni_2P(S)/NF$ [Colour figure can be viewed at wileyonlinelibrary.com]

Figure 3 presents the XPS spectra obtained for $Ni_2P(S)/NF$. The existence of Ni, P and S in the $Ni_2P(S)$ nanowires was confirmed in the survey spectrum (Figure 3A). The C and O may originate from the reference and air contact, respectively.[26,38] Figure 3B shows that two spin-orbit doublets with the binding energies of 852.7/870.0 and 857.5/873.9 eV can be deconvoluted from the high-resolution spectrum obtained for Ni 2p and assigned to $Ni^{\delta+}$ in Ni_2P ($0 < \delta < 2$) and Ni^{2+} arising from oxidation of the Ni species, respectively.[39-41] In the high-magnification XPS spectrum of P 2p (Figure 3C), the lower peaks centered at 130.2 and 131.1 eV were assigned to P $2p_{3/2}$ and P $2p_{1/2}$ in Ni_2P, respectively, with a positive shift,[15,22,42,43] while the peak at 132.6 eV may be attributed to the oxidized P species arising from the superficial oxidation of Ni_2P.[42] As reported previously, the peaks observed at 160.7 and 161.9 eV in the S 2p spectrum can be ascribed to the low coordination sulfur ions on the surface and metal-sulfur bonds, respectively, but there is a negative shift (Figure 3D).[38,44-46] The interaction between P and S may be responsible for the shift in the binding energies of P 2p and S 2p. In other words, the introduction of S changes the charge environment of P, resulting in a change in the catalytic performance.[47]

$Ni_2P(S)/NF$ was used as a freestanding electrode to evaluate the electrochemical HER activity in 1.0 M KOH solution. Bare NF, Ni_2P/NF and Pt/C-NF were also tested for comparison. Figure 4A shows that Pt/C-NF undoubtedly exhibits the best performance, while bare NF exhibits the worst. It can be seen that $Ni_2P(S)/NF$ also shows excellent electrocatalytic performance with a low onset potential of −36 mV, and small overpotentials of 109, 129, and 171 mV used to drive current densities of 10, 20 and 100 $mA{\cdot}cm^{-2}$, respectively. To reach the same

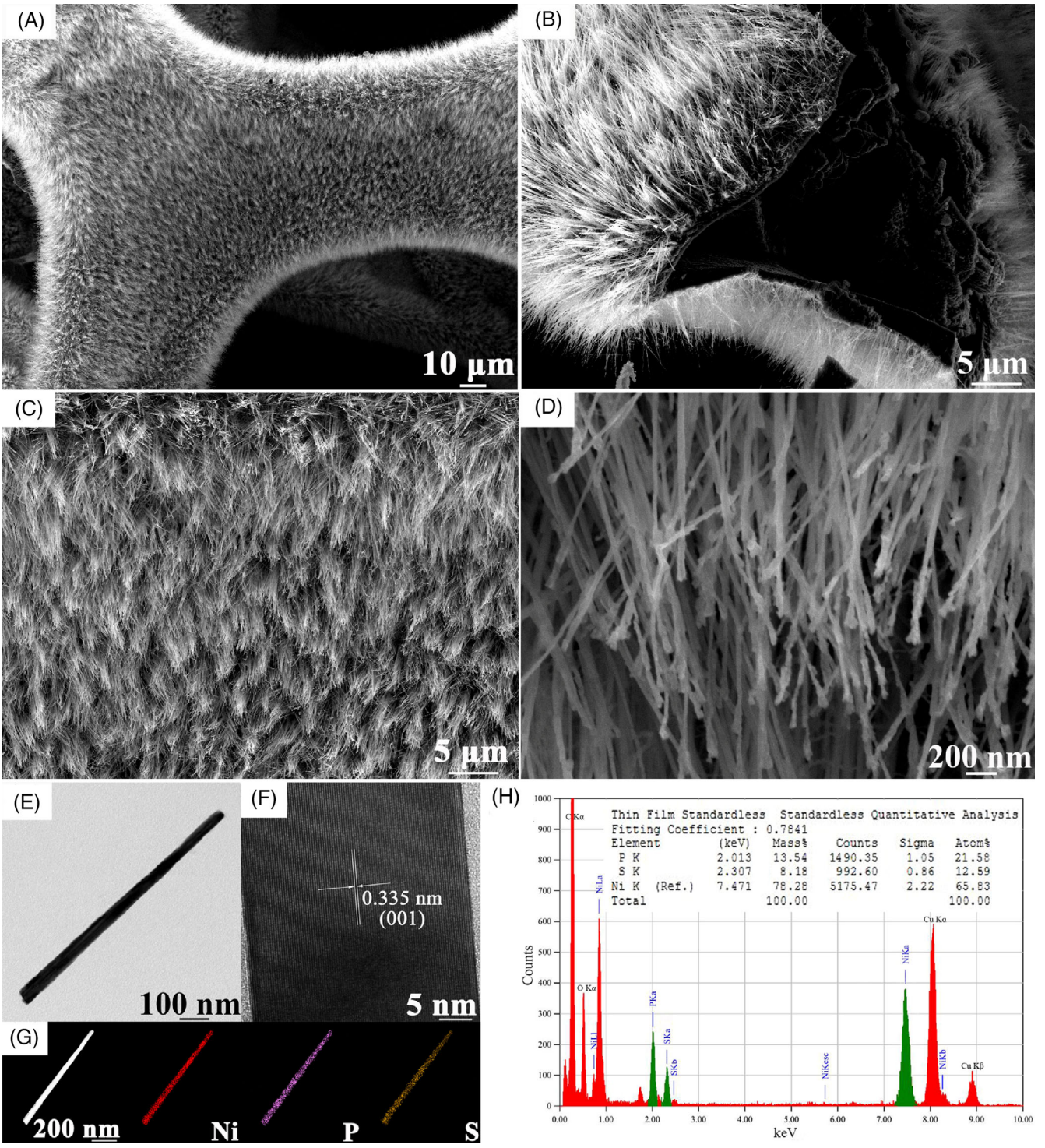

FIGURE 2 A-D, Scanning electron microscopy (SEM) images of $Ni_2P(S)$/NF with different magnification; E, transmission electron microscopy (TEM) and F, high-resolution TEM of single $Ni_2P(S)$ nanowire; G, TEM-EDS mapping and H, spectrum of $Ni_2P(S)$ nanowire. EDS, energy-dispersive X-ray spectroscopy [Colour figure can be viewed at wileyonlinelibrary.com]

current densities, Ni_2P/NF requires much higher overpotentials of 202, 229 and 281 mV, respectively. Moreover, the catalytic activity of $Ni_2P(S)$/NF is preferable or comparable to those of some previously reported Ni-based electrocatalysts, such as $NiSe_2$@NC-PZ (η_{10} = 162 mV),[48] Ni_3S_2@$Ni(OH)_2$/NF(η_{10} = 237 mV),[49] porous Cu-supported Ni-P/CeO_2 (η_{10} = 118 mV),[50] Co-Ni-S-P/graphene (η_{10} = 117 mV),[37] NiCoP/rGO (η_{10} = 209 mV),[14] graphitic N to Ni@CNTs (η_{10} = 244 mV)[51] and MoS_x/Ni-metal-organicframework-

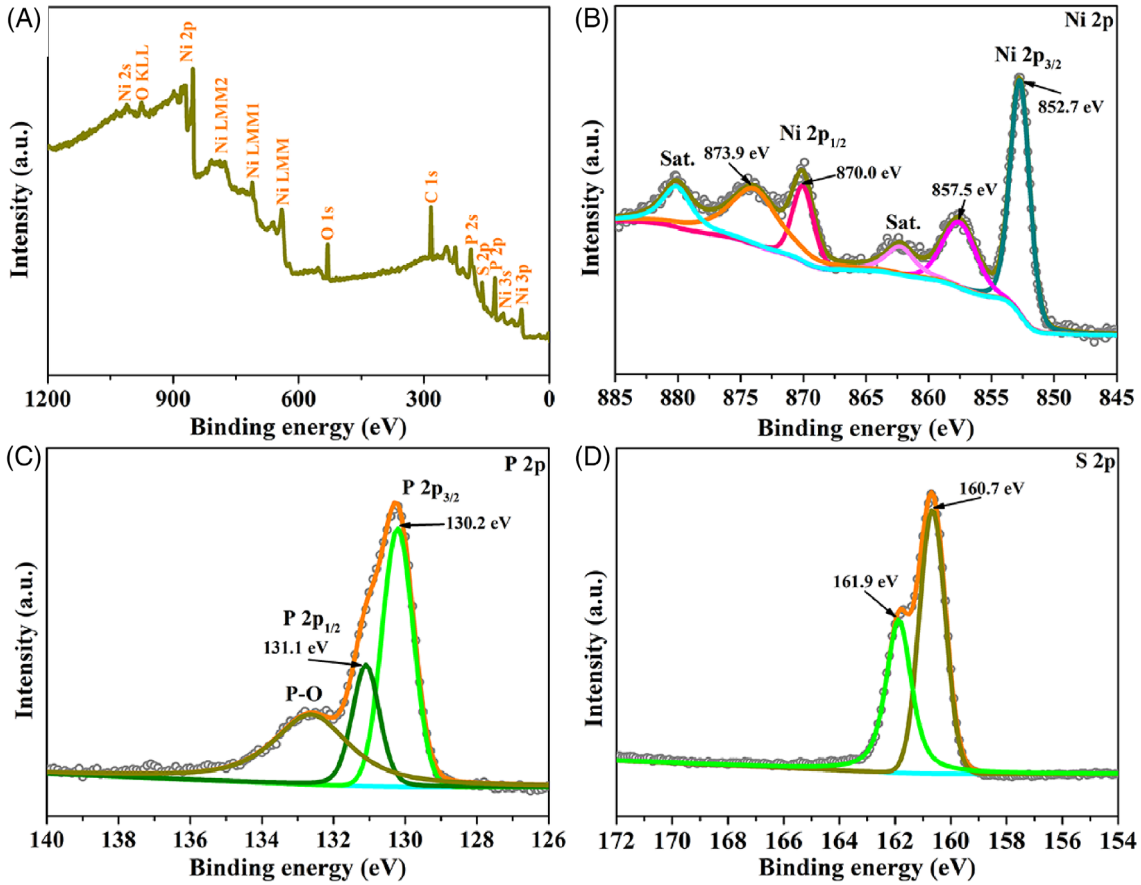

FIGURE 3 A, X-ray photoemission spectrometry (XPS) survey spectrum; high-magnification spectra of B, Ni 2p region; C, P 2p region and D, S 2p region for $Ni_2P(S)/NF$ [Colour figure can be viewed at wileyonlinelibrary.com]

74 composites ($\eta_{10} = 167$ mV).[52] The corresponding Tafel slopes were calculated to evaluate the HER kinetics. Figure 4B shows the bare NF, Ni_2P/NF, Pt/C-NF and $Ni_2P(S)/NF$ possess Tafel slopes of 169.2, 116.2, 56.1 and 68.9 mV·dec^{-1}, respectively. The small Tafel slope of $Ni_2P(S)/NF$ implies the rapid enhancement in the hydrogen generation rate upon increasing the overpotential.[11,22,53] A Volmer–Heyrovsky mechanism with the Heyrovsky reaction being the rate-limiting step can also be derived from the value of 68.9 mV·dec^{-1}.[22,54]

The HER process was further analyzed using EIS measurements and their corresponding fitting. Figure 4C shows the Nyquist plots obtained for $Ni_2P(S)/NF$, Ni_2P/NF and NF are composed of straight lines and capacitive semicircles in the low- and high-frequency regions, respectively. Such plots can be fitted using an equivalent circuit consisting of series resistance (R_s), charge transfer resistance (R_{ct}) and constant phase element (see inset of Figure 4C).[55] The results reveal that $Ni_2P(S)/NF$ has a small R_s of 1.2 Ω, which can be attributed to the in situ growth of the $Ni_2P(S)$ nanowires on the NF substrate. The R_{ct} is usually used to assess the kinetics of the electrochemical reactions occurring on the surface of a catalyst. The smallest R_{ct} value was observed for $Ni_2P(S)/NF$ (4.4 Ω) when compared to Ni_2P /NF (7.7 Ω) and NF (24.5 Ω), which suggests the fastest HER kinetics occur at the interface between $Ni_2P(S)/NF$ and KOH solution.[32,56,57] This may be attributed to two reasons. First, the $Ni_2P(S)$ possesses a higher intrinsic activity. Second, the 1D nanowires with a large aspect ratio were well distributed on the porous 3D NF substrate, which can increase the contact area between the catalyst and electrolyte. Therefore, $Ni_2P(S)/NF$ exhibits a remarkable interfacial reaction rate.

To investigate the catalytic activity in depth, the electrochemical surface area (ECSA) was estimated using the C_{dl}. The CV curves obtained at different scanning rates are shown in Figure S4. From a plot of the difference in the current density between the anodic and cathodic sweeps (Δj) at the middle potential against the scan rates ($\Delta j = j_{anodic} - j_{cathodic}$), it can be seen that the resulting linear slope was twice of the C_{dl} value. The C_{dl} values observed for the different electrodes are presented in Figure 4D. It can be seen that the C_{dl} value of $Ni_2P(S)/NF$ was approximately 109.7 mF·cm^{-2}. However, the C_{dl} values of Ni_2P/NF and NF were only 12.7 and 0.92

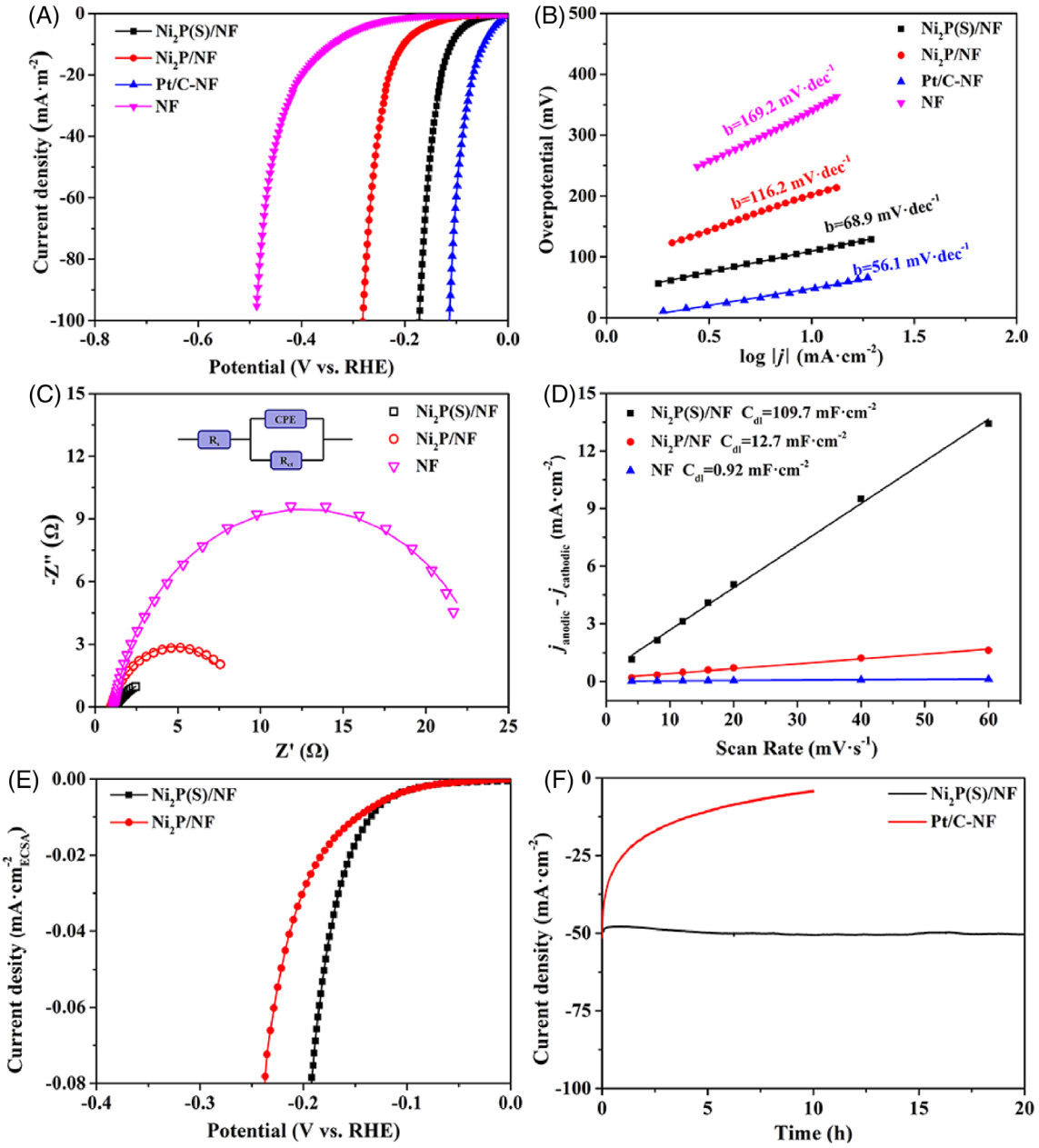

FIGURE 4 A, Polarization curves; B, Tafel plots; C, Nyquist plots; and D, C_{dl} of different catalytic electrodes. E, Polarization curves of Ni_2P(S)/NF and Ni_2P/NF are normalized by ECSA; F, Potentiostatic test of Ni_2P/NF and Pt/C-NF. All of the tests were performed in 1.0 M KOH solution [Colour figure can be viewed at wileyonlinelibrary.com]

$mF{\cdot}cm^{-2}$, respectively, which were much smaller than that of Ni_2P(S)/NF. The large C_{dl} of Ni_2P(S)/NF represents its large ECSA which can be attributed to the 1D nanowires grown on the NF. Therefore, more active sites can be provided by Ni_2P(S)/NF in the catalytic reaction. The catalytic current densities were then normalized using the corresponding ECSAs to investigate their intrinsic activities. The ECSAs were determined by dividing the C_{dl} value by 40 $\mu F{\cdot}cm^{-2}$ (ECSA = C_{dl}/40), because the C_{dl} of a flat surface (1 cm^2) is generally between 20 and 60 $\mu F{\cdot}cm^{-2}$.[11] Figure 4E shows the larger current density observed for Ni_2P(S)/NF when compared to Ni_2P/NF at the same overpotential, which suggests the higher intrinsic catalytic activity of S-substituted Ni_2P.

The durability of Ni_2P(S)/NF was investigated using a potentiostatic method, then measured the HER polarization curve of Ni_2P(S)/NF once again after the potentiostatic test. Figure 4F shows that the current density exhibits an almost a smooth line with time, and Figure S5 suggests that the HER activity decreases little after the potentiostatic test. Although Pt/C-NF exhibited excellent catalytic performance for HER in alkaline

solution, its stability is not good. Figure 4F shows the performance of Pt/C-NF has been significantly reduced under constant potential polarization. The SEM and TEM images (Figure S6A,B) indicate that the morphology and the phases of Ni_2P(S)/NF have no obviously changed after the potentiostatic test. However, the TEM images of Pt/C-NF show Pt nanoparticles are detached from carbon after the potentiostatic test (Figure S7). The difference of morphology before and after long-term catalysis of Ni_2P/NF and Pt/C-NF is one of the reasons for their different durability. These results demonstrate the excellent long-term HER catalytic durability of Ni_2P(S)/NF in an alkaline medium because 1D nanowires with a large aspect ratio are beneficial for releasing bubbles on the surface.[3]

Ni_2P(S)/NF also shows enhanced HER activity when compared to Ni_2P/NF in acid solution. Figure S8A shows Ni_2P/NF requires 184, 204 and 247 mV to drive current densities of 10, 20 and 100 mA·cm^{-2}, respectively. However, Ni_2P(S)/NF only requires 145, 167 and 208 mV to reach the same current densities, respectively. The Tafel slop of Ni_2P(S)/NF is also smaller than that of Ni_2P/NF (see Figure S8B). The enhanced HER activity of Ni_2P(S)/NF in acid solution can be attributed to S-substitution and the optimized morphology.

DFT calculations based on VASP package were performed to calculate the surface adsorption energy of atom H and molecular H_2O to further understand the activity enhancement mechanism and the role of S-substitution. The TEM-EDS results show that approximately 35% of the P sites were substituted by S in the Ni_2P nanowire. Therefore, the atomic ratio of S:P was chosen to be 2:4 in the Ni_2P(S) model for the calculations. The optimized structures obtained for Ni_2P(S) adsorbing H and H_2O on the (001) surface are shown in Figure 5A,B. It is well known that the catalytic activity in the HER can be determined using the free energy of hydrogen adsorption (ΔG_{H^*}),[28,58,59] and the ideal HER catalyst can be achieved under thermo-neutral conditions ($|\Delta G_{H^*}| \approx 0$). The calculated results (Figure 5C) show that the ΔG_{H^*} of Ni_2P(S) (−0.278 eV) is closer to zero when compared to Ni_2P (−0.398 eV), suggesting that Ni_2P(S) has enhanced intrinsic catalytic activity.[28] On the other hand, H_2O is the only proton donor for the HER in an alkaline solution, so the adsorption energy of H_2O (ΔE_{H_2O}) has a significant effect on the catalytic cycle.[59-61] The calculation results obtained for ΔE_{H_2O} are presented in Figure 5D, which demonstrate that Ni_2P(S) exhibits a lower ΔE_{H_2O} value than that of Ni_2P (−5.223 vs −0.336 eV),

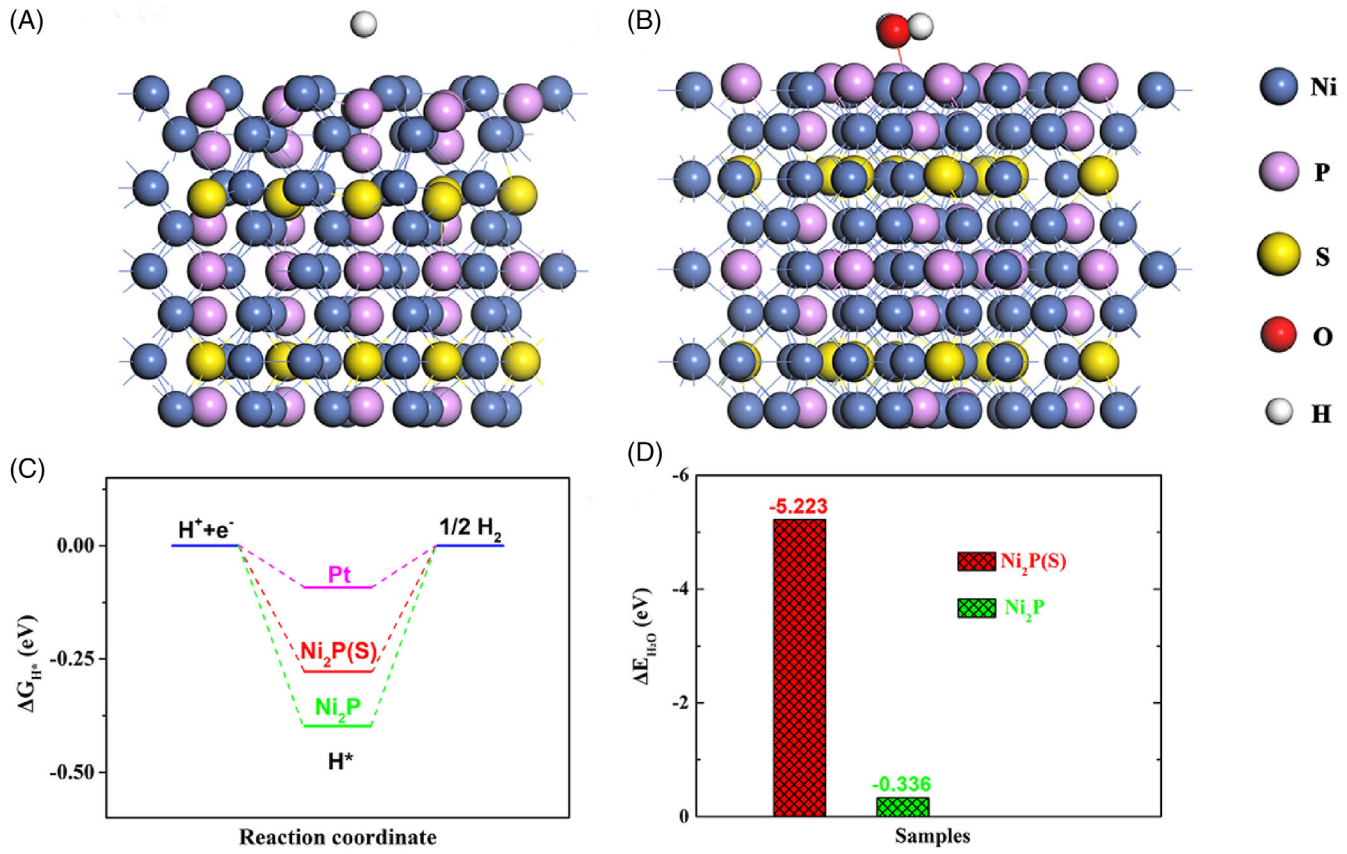

FIGURE 5 The models of Ni_2P(S) adsorbing A, H and B, H_2O on surface; C, ΔG_{H^*} and D, ΔE_{H_2O} of Ni_2P(S) and Ni_2P [Colour figure can be viewed at wileyonlinelibrary.com]

allowing efficient adsorption of H_2O molecules. In a word, DFT calculations confirm that the introduction of S not only makes Ni_2P(S) exhibits a more suitable free energy of hydrogen adsorption but also enhances the H_2O binding activity of Ni_2P(S). Hence, Ni_2P(S)/NF exhibited enhanced activity in HER performed both in alkaline and acidic media.

4 | CONCLUSIONS

In summary, S-substituted Ni_2P nanowires with large aspect ratios have been successfully grown on nickel foam using phosphating-sulfurised nickel foam prepared via a low-temperature heat treatment process. The Ni_2P(S)/NF, as a 3D self-supporting electrode, exhibited excellent HER electrocatalytic performance both in alkaline and acidic media. To drive current densities of 100 $mA{\cdot}cm^{-2}$, Ni_2P(S)/NF only requires low overpotentials of 171 and 208 mV in 1.0 M KOH and 0.5 M H_2SO_4 solution, respectively. The characterization studies and DFT calculations indicate that this superior catalytic activity can be attributed to: (a) The in situ growth of nanowires on nickel foam, which not only allows good mechanical adhesion between the catalyst and substrate but also avoids aggregation or re-stacking; (b) the morphology of the 1D nanowires with a high length-to-diameter ratio on a 3D substrate exposes abundant catalytic active sites and favors ion/electron transfer. (c) Ni_2P(S) has a more thermal-neutral-free energy of hydrogen adsorption and higher H_2O binding activity when compared to Ni_2P. Due to its superior performance, Ni_2P(S)/NF will hopefully be used for low-cost hydrogen production using water electrolysis.

ACKNOWLEDGEMENTS

We thank the Science and Technology Strategic Cooperation Programs of Luzhou Municipal People's Government and Southwest Medical University (Grant No. 2019LZXNYDJ18); Natural Science Foundation of Sichuan Province (Grant No. 14JC0124) and Natural Science Foundation of Shaanxi Province (Grant No. 2020JQ-386) for funding.

ORCID

Yun Zhou https://orcid.org/0000-0002-5032-9467

REFERENCES

1. Møller KT, Jensen TR, Akiba E, Li HW. Hydrogen—a sustainable energy carrier. *Prog Nat Sci Mater*. 2017;27(1):34-40.
2. Hosseini SE, Wahid MA. Hydrogen production from renewable and sustainable energy resources: promising green energy carrier for clean development. *Renew Sustain Energy Rev*. 2016;57:850-866.
3. Nikolaidis P, Poullikkas A. A comparative overview of hydrogen production processes. *Renew Sustain Energy Rev*. 2017;67:597-611.
4. Hosseini SE, Wahid MA. Hydrogen from solar energy, a clean energy carrier from a sustainable source of energy. *Int J Energy Res*. 2020;44(6):4110-4131.
5. Tang S, Liu Y, Lei A. Electrochemical oxidative cross-coupling with hydrogen evolution: a green and sustainable way for bond formation. *Chem*. 2018;4(1):27-45.
6. da Silva VT, Mozer TS, da Silva César A. Hydrogen: trends, production and characterization of the main process worldwide. *Int J Hydrogen Energy*. 2017;42(4):2018-2033.
7. Razi F, Dincer I. A critical evaluation of potential routes of solar hydrogen production for sustainable development. *J Clean Prod*. 2020;264:121582.
8. Gençer E. Exploring the rapidly changing energy system. *Electric Power*. 2019;3:3.
9. Fang M, Gao W, Dong G, et al. Hierarchical NiMo-based 3D electrocatalysts for highly-efficient hydrogen evolution in alkaline conditions. *Nano Energy*. 2016;27:247-254.
10. Deng J, Ren P, Deng D, Yu L, Yang F, Bao X. Highly active and durable non-precious-metal catalysts encapsulated in carbon nanotubes for hydrogen evolution reaction. *Energ Environ Sci*. 2014;7(6):1919-1923.
11. Yang Y, Zhang K, Lin H, et al. MoS_2-Ni_3S_2 heteronanorods as efficient and stable bifunctional electrocatalysts for overall water splitting. *ACS Catal*. 2017;7:2357-2366.
12. Feng L-L, Yu G, Wu Y, et al. High-index faceted Ni_3S_2 nanosheet arrays as highly active and ultrastable electrocatalysts for water splitting. *J Am Chem Soc*. 2015;137:14023-14026.
13. Staszak-Jirkovský J, Malliakas C, Lopes P, et al. Design of active and stable Co-Mo-S_x chalcogels as pH-universal catalysts for the hydrogen evolution reaction. *Nat Mater*. 2016;15(2):197-203.
14. Li J, Yan M, Zhou X, et al. Mechanistic insights on ternary $Ni_{2-x}Co_xP$ for hydrogen evolution and their hybrids with graphene as highly efficient and robust catalysts for overall water splitting. *Adv Funct Mater*. 2016;26(37):6785-6796.
15. Zhang X, Gu W, Wang E. Wire-on-flake heterostructured ternary $Co_{0.5}Ni_{0.5}P$/CC: an efficient hydrogen evolution electrocatalyst. *J Mater Chem A*. 2017;5:982-987.
16. Wu T, Pi M, Zhang D, Chen S. 3D structured porous CoP_3 nanoneedle arrays as an efficient bifunctional electrocatalyst for the evolution reaction of hydrogen and oxygen. *J Mater Chem A*. 2016;4:14539-14544.
17. Wang T, Wang X, Liu Y, Zheng J, Li X. A highly efficient and stable biphasic nanocrystalline Ni-Mo-N catalyst for hydrogen evolution in both acidic andalkaline electrolytes. *Nano Energy*. 2016;22:111-119.
18. Jin H, Gu Q, Chen B, et al. Molten salt-directed catalytic synthesis of 2D layered transition-metal nitrides for efficient hydrogen evolution. *Chem*. 2020;6(9):2382-2394.
19. Lin H, Shi Z, He S, et al. Heteronanowires of MoC-Mo_2C as efficient electrocatalysts for hydrogen evolution reaction. *Chem Sci*. 2016;7:3399-3405.
20. Wan C, Regmi YN, Leonard BM. Multiple phases of molybdenum carbide as electrocatalysts for the hydrogen evolution reaction. *Angew Chem*. 2014;126:6525-6528.

21. Qu G, Zhao Y, Zhao G, et al. Ultrahigh length-to-diameter ratio nickel phosphide nanowires as pH-wide electrocatalyst for efficient hydrogen evolution. *Electrochim Acta*. 2019;298:943-949.
22. Wen L, Yu J, Xing C, et al. Flexible vanadium-doped Ni_2P nanosheet arrays grown on carbon cloth for an efficient hydrogen evolution reaction. *Nanoscale*. 2019;11(10):4198-4203.
23. Sun Y, Hang L, Shen Q, et al. Mo doped Ni_2P nanowire arrays: an efficient electrocatalyst for the hydrogen evolution reaction with enhanced activity at all pH values. *Nanoscale*. 2017;9(43):16674-16679.
24. Jiang B, Ban X, Wang Q, et al. Anionic P-substitution toward ternary Ni–S–P nanoparticles immobilized graphene with ultrahigh rate and long cycle life for hybrid supercapacitors. *J Mater Chem A*. 2019;7:24374-24388.
25. Zhang H, Jiang H, Hu Y, Jiang H, Li C. Integrated Ni-P-S nanosheets array as superior electrocatalysts for hydrogen generation. *Green Energy Environ*. 2017;2:112-118.
26. Zhang X, Zhang S, Li J, Wang E. One-step synthesis of well-structured NiS–$Ni_2P_2S_6$ nanosheets on nickel foam for efficient overall water splitting. *J Mater Chem A*. 2017;5:22131-22136.
27. Dai Z, Geng H, Wang J, et al. Hexagonal-phase cobalt monophosphosulfide for highly efficient overall water splitting. *ACS Nano*. 2017;11(11):11031-11040.
28. Zeng L, Sun K, Wang X, et al. Three-dimensional-networked Ni_2P/Ni_3S_2 heteronanoflake arrays for highly enhanced electrochemical overall-water-splitting activity. *Nano Energy*. 2018;51:26-36.
29. Cabán-Acevedo M, Stone ML, Schmidt JR, et al. Efficient hydrogen evolution catalysis using ternary pyrite-type cobalt phosphosulphide. *Nat Mater*. 2015;14(12):1245-1125.
30. Huang S, Zhang W, Cui S, Chen W, Mi L. Sequential partial ion exchange synthesis of composite Ni_3S_2/Co_9S_8/NiSe nanoarrays with a lavender-like hierarchical morphology. *Inorg Chem Front*. 2017;4:727-735.
31. Yang W, Tian J, Hou L, et al. Hierarchical MoP hollow nanospheres anchored on a N, P, S-doped porous carbon matrix as efficient electrocatalysts for the hydrogen evolution reaction. *ChemSusChem*. 2019;12(20):4662-4670.
32. Li W, Xiong D, Gao X, Song WG, Xia F, Liu L. Self-supported Co-Ni-P ternary nanowire electrodes for highly efficient and stable electrocatalytic hydrogen evolution in acidic solution. *Catal Today*. 2017;287:122-129.
33. Wang X-D, Chen H-Y, Xu Y-F, et al. Self-supported $NiMoP_2$ nanowires on carbon cloth as an efficient and durable electrocatalyst for overall water splitting. *J Mater Chem A*. 2017;5:7191-7199.
34. Zhang L, Wang T, Sun L, et al. Hydrothermal synthesis of 3D hierarchical $MoSe_2/NiSe_2$ composite nanowires on carbon fiber paper and their enhanced electrocatalytic activity for the hydrogen evolution reaction. *J Mater Chem A*. 2017;5:19752-19759.
35. Grimme S. Semiempirical GGA-type density functional constructed with a long-range dispersion correction. *J Comput Chem*. 2006;27(15):1787-1799.
36. Perdew JP, Burke K, Ernzerhof M. Generalized gradient approximation made simple. *Phys Rev Lett*. 1996;77(18):3865-3868.
37. Song HJ, Yoon H, Ju B, et al. 3D architectures of quaternary Co-Ni-S-P/grapheme hybrids as highly active and stable bifunctional electrocatalysts for overall water splitting. *Adv Energy Mater*. 2018;8(33):1802319.
38. Wu X, Li S, Wang B, Liu J, Yu M. $NiCo_2S_4$ nanotube arrays grown on flexible nitrogen-doped carbon foams as three dimensional binder-free integrated anodes for high-performance lithium-ion batteries. *Phys Chem Chem Phys*. 2016;18:4505-4512.
39. Tang C, Zhang R, Lu W, et al. Energy-saving electrolytic hydrogen generation: Ni_2P nanoarray as a high-performance non-noble-metal electrocatalyst. *Angew Chem*. 2017;129:860-864.
40. Liang X, Zheng B, Chen L, Zhang J, Zhuang Z, Chen B. MOF-derived formation of Ni_2P-CoP bimetallic phosphides with strong interfacial effect toward electrocatalytic water splitting. *ACS Appl Mater Interfaces*. 2017;9:23222-23229.
41. Wang Q, Liu Z, Zhao H, Huang H, Jiao H, du Y. MOF-derived porous Ni_2P nanosheets as novel bifunctional electrocatalysts for the hydrogen and oxygen evolution reactions. *J Mater Chem A*. 2018;6(38):18720-18727.
42. Lin Y, He L, Chen T, et al. Cost-effective and environmentally friendly synthesis of 3D Ni_2P from scrap nickel for highly efficient hydrogen evolution in both acidic and alkaline media. *J Mater Chem A*. 2018;6(9):4088-4094.
43. Wu C, Kopold P, Aken PAV, et al. High performance graphene/Ni_2P hybrid anodes for lithium and sodium storage through 3D yolk–shell-like nanostructural design. *Adv Mater*. 2017;29:1604015.
44. Zhang H, Guan B, Gu J. One-step synthesis of nickel cobalt sulphides particles: tuning the composition for high performance supercapacitors. *RSC Adv*. 2016;6:58916-58924.
45. Zhang Z, Wang Q, Zhao C, Min S, Qian X. One-step hydrothermal synthesis of 3D petal-like Co_9S_8/RGO/Ni_3S_2 composite on nickel foam for high-performance supercapacitors. *ACS Appl Mater Interfaces*. 2015;7:4861-4868.
46. Pu J, Cui F, Chu S, Wang T, Sheng E, Wang Z. Preparation and electrochemical characterization of hollow hexagonal $NiCo_2S_4$ nanoplates as pseudocapacitor materials. *ACS Sustainable Chem Eng*. 2014;2:809-815.
47. Song H, Dai X, Zhu T, et al. Effect of boron promoter on structure and hydrogenation activity of Ni_2P/MCM-41 catalysts. *J China Univ Petroleum*. 2019;43(5):170-177.
48. Huang Z, Yuan S, Zhang T, et al. Selective selenization of mixed-linker Ni-MOFs: $NiSe_2$@ NC core-shell nano-octahedrons with tunable interfacial electronic structure for hydrogen evolution reaction. *Appl Catal B-Environ*. 2020;272:118976.
49. Hao S, Cao Q, Yang L, Che R. Morphology-optimized interconnected Ni_3S_2 nanosheets coupled with $Ni(OH)_2$ nanoparticles for enhanced hydrogen evolution reaction. *J Alloy Comp*. 2020;827:154163.
50. Zhou Q, Liu S, Zhang Y, Zhu Z, Su W, Sheng M. Fabrication of porous cu supported Ni-P/CeO_2 composite coatings for enhanced hydrogen evolution reaction in alkaline solution. *Ceram Int*. 2020;46(13):20871-20877.
51. Oluigbo CJ, Ullah N, Xie M, et al. Incorporation of pyridinic and graphitic N to Ni@CNTs: as a competent electrocatalyst for hydrogen evolution reaction. *Int J Energy Res*. 2020;44(11):9157-9165.
52. Do HH, Le QV, Nguyen TV, et al. Synthesis of MoS_x/Ni-metal-organic framework-74composites as efficient electrocatalysts for hydrogen evolution reactions. *Int J Energy Res*. 2021;45(6):9638-9647.

53. Peng S, Li L, Zhang J, et al. Engineering Co_9S_8/WS_2 array films as bifunctional electrocatalysts for efficient water splitting. *J Mater Chem A*. 2017;5:23361-23368.
54. Yang C, Gao MY, Zhang QB, Zeng JR, Li XT, Abbott AP. In-situ activation of self-supported 3D hierarchically porous Ni_3S_2 films grown on nanoporous copper as excellent pH-universal electrocatalysts for hydrogen evolution reaction. *Nano Energy*. 2017;36:85-94.
55. Sivanantham A, Ganesan P, Shanmugam S. Hierarchical $NiCo_2S_4$ nanowire arrays supported on Ni foam: an efficient and durable bifunctional electrocatalyst for oxygen and hydrogen evolution reactions. *Adv Funct Mater*. 2016;26:4661-4672.
56. Wang K, Zhou C, Xi D, et al. Component-controllable synthesis of $Co(S_xSe_{1-x})_2$ nanowires supported by carbon fiber paper as high-performance electrode for hydrogen evolution reaction. *Nano Energy*. 2015;18:1-11.
57. Yu J, Li Q, Chen N, et al. Carbon-coated nickel phosphide nanosheets as efficient dual electrocatalyst for overall water splitting. *ACS Appl Mater Interfaces*. 2016;8:27850-27858.
58. Zhang L, Ren X, Guo X, et al. Efficient hydrogen evolution electrocatalysis at alkaline pH by interface engineering of Ni_2P-CeO_2. *Inorg Chem*. 2018;57:548-552.
59. Liu B, Zhao Y-F, Peng H-Q, et al. Nickel–cobalt diselenide 3D mesoporous nanosheet networks supported on Ni foam: an all-pH highly efficient integrated electrocatalyst for hydrogen evolution. *Adv Mater*. 2017;29:1606521.
60. Liu T, Ma X, Liu D, et al. Mn doping of CoP nanosheets array: an efficient electrocatalyst for hydrogen evolution reaction with enhanced activity at all pH values. *ACS Catal*. 2017;7:98-102.
61. Zou X, Zhang Y. Noble metal-free hydrogen evolution catalysts for water splitting. *Chem Soc Rev*. 2015;44(15):5148-5180.

SUPPORTING INFORMATION

Additional supporting information may be found online in the Supporting Information section at the end of this article.

How to cite this article: Xu J, Li T, Zhang L, He B, Feng D, Zhou Y. One-step synthesis of anionic S-substitution toward $Ni_2P(S)$ nanowires on nickel foam for enhanced hydrogen evolution reaction. *Int J Energy Res*. 2021;1–11. https://doi.org/10.1002/er.6940